applied sciences

MDPI

Article

Design and Implementation of Three-Phase Smart Inverter of the Photovoltaic Power Generation Systems

Kuo-Hua Huang, Kuei-Hsiang Chao *, Zhi-Yao Sun and Cheng-Yi Ho

Department of Electrical Engineering, National Chin-Yi University of Technology, Taichung 41170, Taiwan
* Correspondence: chaokh@ncut.edu.tw; Tel.: +886-4-2392-4505 (ext. 7272); Fax: +886-4-2392-2156

Abstract: The main purpose of this paper is to conduct design and implementation on three-phase smart inverters of the grid-connected photovoltaic system, which contains maximum power point tracking (MPPT) and smart inverter with real power and reactive power regulation for the photovoltaic module arrays (PVMA). Firstly, the piecewise linear electrical circuit simulation (PLECS) power electronic real-time control system was applied to construct the simulation and actual test environment for the three-phase mains parallel photovoltaic system, where the KC200GT photovoltaic module was used to form a 1600 W system for conducting the simulation. For enabling the PVMA to output the maximum power in terms of both insolation and ambient temperature, where the perturbation and observation (P&O) method was used for MPPT. Then, the voltage-power control technology was added to the grid-connected photovoltaic inverter. When the grid voltage p.u. value is between 1.0 and 1.03, the smart inverter starts voltage-power regulation, reducing the real power output to 1440 W, and absorbing the system's reactive power to 774 VAr. The power factor of the grid system end is controlled to 0.9 (lagging), and the grid voltage is reduced to norminal value 220 V. If the grid voltage p.u. value is between 0.97 and 1.0, the smart inverter starts voltage-power regulation, controlling the output real power to 1440 W and the reactive power to the system to 774 VAr, so that the power factor of the system end is controlled to 0.9 (leading), and the grid voltage is increased to norminal value 220 V. Finally, the results from the simulation and actual test were used to demostrate the effectiveness of the regulation performance of the smart inverter.

Keywords: photovoltaic system; maximum power point tracking (MPPT); photovoltaic grid-connected smart inverter; voltage-power regulation

check for updates

Citation: Huang, K.-H.; Chao, K.-H.; Sun, Z.-Y.; Ho, C.-Y. Design and Implementation of Three-Phase Smart Inverter of the Photovoltaic Power Generation Systems. *Appl. Sci.* **2023**, *13*, 294. https://doi.org/10.3390/app13010294

Academic Editor: Giovanni Petrone

Received: 26 October 2022
Revised: 13 December 2022
Accepted: 24 December 2022
Published: 26 December 2022

1. Introduction

The energy storage system is usually suitable for reducing the workload of the power supply system during peak periods of power consumption. Mostly, the problem of insufficient power supply is solved by other alternative energy, such as batteries and photovoltaic systems. In order to convert the energy from energy storage systems or photovoltaic systems into electrical energy that can be utilized by general electrical appliances, the power conditioner must be used for power conversion. Since the PVMA is significantly affected by the insolation and the module temperature, the relationship between the output voltage and current is nonlinear. Therefore, the characteristic curve also differs under different insolation and module temperature. Therefore, the MPPT technique shall be applied to the photovoltaic system to reach maximum power output. In addition, due to unstable direct current (DC) output from the photovoltaic system, the DC must be converted into stable alternating current (AC) by the inverter, which then connects with mains in parallel for power supply. When the power supply from general mains parallel photovoltaic power generation system is insufficient for residential consumption, residents can fill up the power insufficiency from mains. In the case of residual conversion power in the photovoltaic power generation system, it can be sold to the power company for rebates. Thus, in addition to reducing the demand in peak consumption of mains, such a system can also mitigate the power company's need to increase power generators due to only a few hours of daily supply in peak power consumption. At the same time, the CO_2 produced from coal burning can also be reduced. The advantages of a grid-connected photovoltaic system lay in the system simplicity, ease of maintenance, and the conversion efficiency of the photovoltaic inverter can reach 98%. The grid-connected photovoltaic inverter can convert the photovoltaic DC voltage output from the maximum power tracker into sine AC voltage and supply power to the mains grid. The magnitude, frequency, and phase of the output voltage are controlled to be consistent with the mains grid, where the power factor is controlled at 1.

However, should a massive amount of the photovoltaic power generation system connect with the mains system in parallel, the characteristics of changing along with insolation and module temperature will cause tremendous variation in the mains voltage and reduce the power quality of the mains system. Therefore, the smart inverter needs to be utilized to control the real power and reactive power for steady voltage in the power supply. In order to enhance the control performance of smart inverters to improve the quality of grid power, many scholars have conducted numerous research [1–3] on the subject over recent years. If the real power unlimitedly feeds into the power grid, it may cause severe voltage fluctuation. Therefore, the literature [1] conducted research on control methods for grid-connected inverters, where the control strategy is based on a deep neural network (DNN). The voltage of the grid-connected point for the inverter was trained regularly, so the control performance of the smart inverter could be enhanced. Under such a method, since training samples were utilized to achieve the DNN control strategy; thus, the requirements of hardware performance were higher and caused an increase in cost. The literature [2] optimized the control methods of the photovoltaic smart inverters. The voltage-power control technique proposed was combined with slime mould algorithm (SMA) for controlling purposes, which enhanced the carrying capacity and power quality for the photovoltaic power generation system in the grid. However, the disadvantage lies in relative complications in calculations. The literature [3] focused on the current controller of the multilevel neutral point clamped (NPC) inverter for photovoltaic power generation, where the hysteresis current controller is based on a space vector was proposed. In addition to transmitting the real power of the photovoltaic module array to a grid-connected system, the controller could also compensate for the harmonic current and reactive power at the same time; however, the control methods were extensively complicated. Based on the above, a simple and effective control method was proposed regarding the adjustment of real and reactive power for MPPT and smart inverter of the photovoltaic power generation system. Therefore, in this paper, a proportional-integral (P-I) controller commonly used in the industry is used to control the DC-link voltage and the real and reactive power of the smart inverter. Although its control performance is less robust than that of the intelligent controller, it can shorten the operation time of the controller and improve the response speed.

The arrangement of the various section contents is as follows: Section 2 describes the maximum power point tracking algorithm for the photovoltaic system and the circuit design of the boost converter. Section 3 describes the smart inverter control architecture, including DC-link voltage control, output power control and voltage-power control. The simulation and actual test results of the three-phase photovoltaic smart inverter for three per-unit values of the main voltage were made in Section 4 to verify the effectiveness of the developed smart inverter. Finally, the conclusion of this paper describes the results of this work.

2. The MPPT for Photovoltaic System

In this paper, the PLECS power electronic real-time control system developed by Plexim GmbH Co., Ltd. [4] was applied to establish the equivalent circuit model of the photovoltaic module that has the same output characteristic curve as the photovoltaic module KC200GT [5] under the actual operation. The modules are then connected as 4 in series and 2 in parallel to form a photovoltaic module array of 1600 W with a rated output voltage of 105.2 V and a rated output current of 15.22 A, where the P&O MPPT method was applied [6,7] to track the maximum power point (MPP) under different insolation and module temperature.

2.1. Perturbation and Observation Method

The P&O method is the MPPT algorithm applied most extensively at present. Through the change in the direction of perturbation, the output voltage of the photovoltaic module array is adjusted. The module array output power after perturbation and the power before perturbation are then compared with each other to determine the direction of the next perturbation. From Figures 1 and 2, it can be observed that if the output power tested is greater than the previous power measured ($P_{(k+1)} > P_{(k)}$), when the positive perturbation voltage increases, the positive perturbation continues to increase. Conversely, when the output power tested is less than the previous power measured ($P_{(k+1)} < P_{(k)}$), then change the perturbation direction and repeat the action mentioned above, where the output power can reach the MPP.

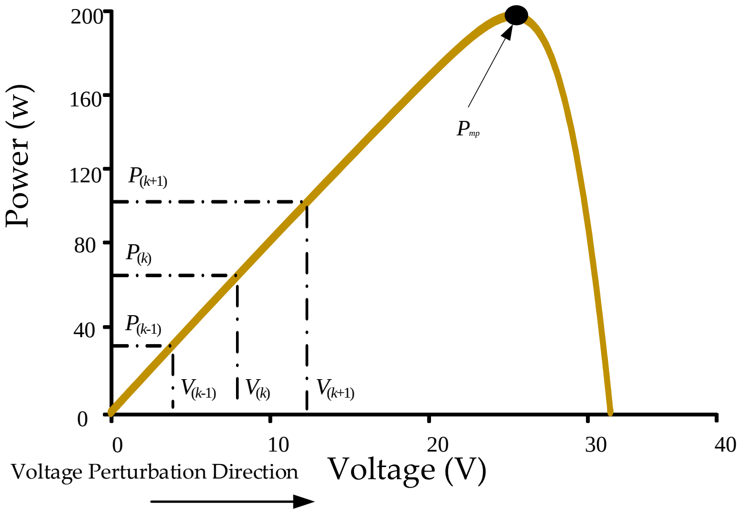

Figure 1. Work illustration for positive perturbation voltage of the perturbation and observation method.

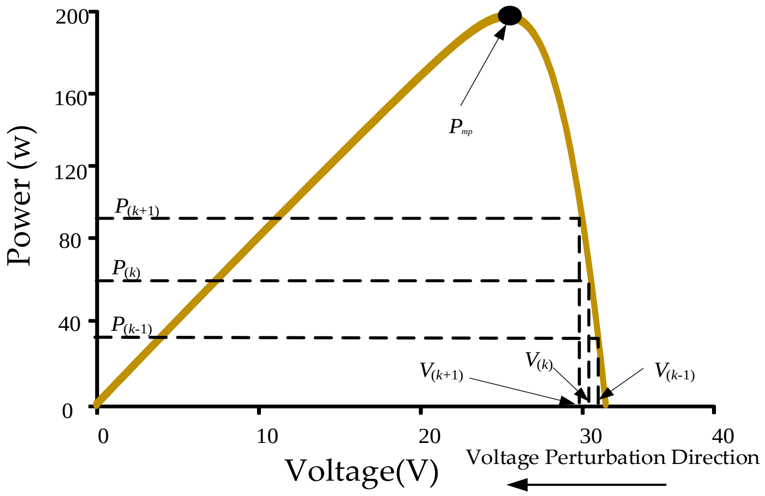

Figure 2. Work illustration for negative perturbation voltage of the perturbation and observation method.

The MPPT method of PVMA is not the main research focus of this paper, but only to effectively regulate the PVMA output maximum power, so as to carry out the adjustment performance test of the smart inverter output real power and reactive power.

2.2. Design of Boost Converter Circuit

The circuit architecture of boost converter [8,9] is shown in Figure 3. It adjusts duty cycle D of the converter, which allows the PVMA to operate on the MPP.

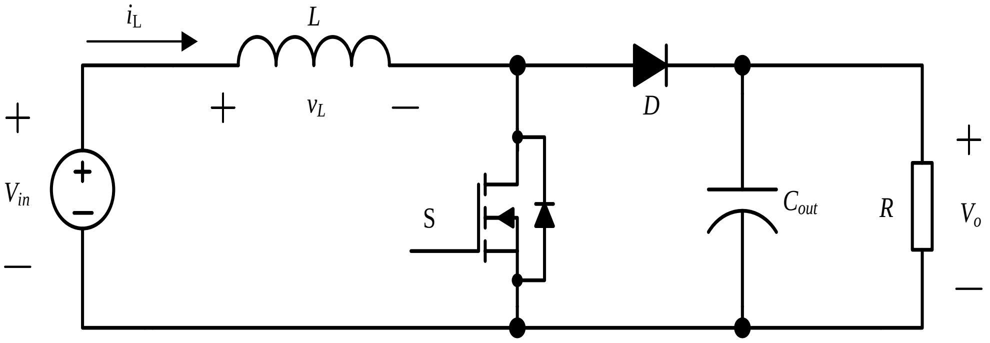

Figure 3. Circuit architecture of boost converter.

The boost converter in this paper is designed with a duty cycle D of the switch for 0~1, which enables the inductor current to work in a continuous conduction mode (CCM). It can be deduced from reference [10] that the inductance value of the boost converter must satisfy the condition of Equation (1). However, the function $D(1-D)^2$ in Equation (1) has a maximum value when D = 1/3. Therefore, it can be known from Equation (1) that if the inductance current is to operate in current CCM when the duty cycle D is between 0 and 1, the required inductance value L is the maximum when D = 1/3. Therefore, the inductance value is the required value when D = 1/3. The converter can be operated in current CCM under all duty cycles. The boost converter used for switching frequency f is 20 kHz, rated power P is 1800 W, and the maximum output voltage V_o is 400 V, so the resistance value of the load R can be calculated from $R = {V_o}^2/P$ is 89 Ω. Therefore, according to Equation (1), when D = 1/3, the required L value can be calculated as 330 μH, and then multiplied by 1.25 times the margin to ensure that the inductor current can be operated in CCM. Therefore, the inductor value chosen in this paper is 0.5 mH.

$$L \geq \frac{D(1-D)^2 R}{2f} \tag{1}$$

Since the change in electrical charge of the filter capacitor during active conduction of the switch was [10]

$$|\Delta Q| = \frac{V_o}{R} DT = C\Delta V_o \tag{2}$$

The filter capacitance derived from Equation (2) was

$$C = \frac{D}{Rf(\Delta V_o/V_o)} \tag{3}$$

where $\Delta V_o/V_o$ was the ripple ratio of output voltage. To usefully reduce the ripple of output voltage, the ripple ratio of the output voltage was set at $\Delta V_o/V_o = 1\%$, and this value was substituted into Equation (3) to obtain the capacitance value of 18.71 μF. Since the withstand voltage of the capacitor should be greater than the output voltage of 400 V and considering the convenience of parts acquisition, a capacitor with a specification of 470 μF/450 V was selected. For the component selection of the switch and the diode, considering that both withstand voltages should be greater than the output voltage of 400 V cutoff and the withstand current of switch component calculated according to [10] should be greater than 4.53 A, as well as the convenience of laboratory acquisition, IRFP460 was selected as the switching component specified at 500 V/20 A. FMPG5FS was selected as the diode specified at 1500 V/10 A.

3. Smart Inverter Control Architecture

In the future, since there will be more and more photovoltaic systems connected to the mains in parallel, the voltage of mains will rise or fall should there be an excessive or insufficient supply of energy to the mains. Then, the smart inverter will control the output power based on the level of mains voltage detected. Through generation or absorption of reactive power over the grid-connected mains to effectively restrain and stabilize the mains voltage at normal value, the adjustment for balanced grid supply and demand is achieved. Regarding research and development (R&D) of the photovoltaic smart inverter, the inverter researched and manufactured as per this paper was specified with input DC voltage at 400 V, output AC voltage at the root-mean-square value of 220 V, and sine wave at a frequency of 60 Hz.

3.1. Control Architecture of Three-Phase Photovoltaic Full-Bridge Inverter

The circuit architecture of the three-phase photovoltaic full-bridge inverter adopted in this paper is shown in Figure 4. The dual-loop P-I controller [11,12] was used, and the outer loop served as the DC-link voltage loop that generated a current command from the error between the DC-link voltage set and then measured. The inner loop served as the inverter output voltage and current control loop, where the error was used to generate the pulse width modulation (PWM) control signal [13–15] for controlling the output voltage and current. With the addition of L_1-C-L_2, the three-level low-pass filter [16,17] forms to attenuate the high-frequency harmonic wave of the inverter, so the output voltage becomes a low-frequency AC sine wave.

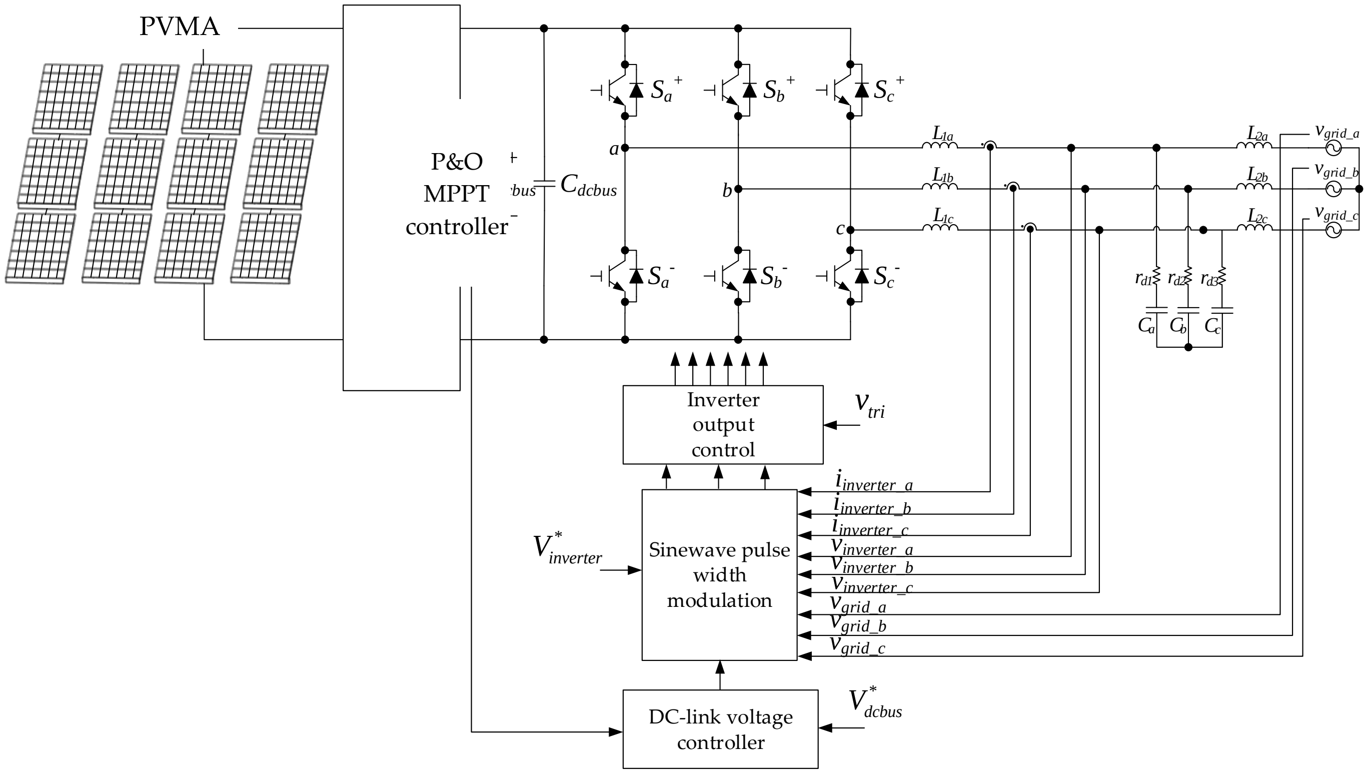

Figure 4. Circuit architecture of three-phase photovoltaic full-bridge inverter.

Compared with the LC filter, the LCL filter requires less inductance to remove low frequency harmonics of the converter. However, the small amount of inductance is smaller, the cost is lower, the system's overall efficiency is not affected, and the dynamic response is better.

As the LCL filter is a third-order filter, it will cause system instability. Therefore, a damping resistor should be connected in series to the capacitor of the LCL filter to avoid oscillation of the system. The damping resistor is divided into a passive and an active damping resistor. For passive damping system, a damping resistor is connected in series to the capacitor to achieve the system's stability, and its control is simple and low-cost; The active damping system achieves the system's stability by controlling the current of the capacitor. Although its efficiency is high, the control is more complicated and expensive. According to the above comparison, this paper adopts the passive damping system with simple system architecture as shown in Figure 4. In addition, the adopted LCL filter with passive damping resistor is relatively easy to realize.

The following will be explained by the design method of the LCL filter of one phase, and the three-phase circuit parameters are equivalent to $L_1 = L_{1a} = L_{1b} = L_{1c}$, $L_2 = L_{2a} = L_{2b} = L_{2c}$, $R_d = r_{d1} = r_{d2} = r_{d3}$ and $C = C_a = C_b = C_c$. Since the output power factor of the general grid-connected system is controlled as 1.0, if the converter adopts the bipolar switching control method, the total inductance of the LCL filter is L_t, which can be obtained from Equation (4) [16,17].

$$L_t = \frac{V_{dc}}{4 I_{rms} f_{sw} \Delta I_{ripple}} (1 - m_a) m_a \tag{4}$$

where V_{dc} is the input DC voltage of the inverter, I_{rms} is the effective (or root-mean-square, RMS) value of the inverter output current, ΔI_{ripple} is the percentage of output current ripple; m_a is the amplitude modulation ratio, and f_{sw} is the switching frequency of the switch. L_t can be rewritten as shown in Equation (5) [16,17].

$$L_t = \frac{L_1 L_2}{L_1 + L_2} \tag{5}$$

Different degrees of harmonic attenuation can be obtained when L_1 and L_2 are distributed in different proportions. The relationship between the two is shown in Equation (6). The proportional parameters α of the two can achieve a better harmonic attenuation effect within the range $4 \leq \alpha \leq 6$, according to the conclusions of the literature [18].

$$L_1 = \alpha L_2 \tag{6}$$

The value α used in this paper is 5, which is substituted into Equation (6) and then back into Equation (5) to obtain L_1 and L_2 values.

The design of capacitors is limited by the reactive power Q generated. Generally speaking, it should not exceed 5% of the output-rated power P_{out}, then the capacitance value can be calculated through Equation (7) [19].

$$C \leq \frac{Q}{\omega_o {V_{rms}}^2} = \frac{0.05 P_{out}}{\omega_o {V_{rms}}^2} \tag{7}$$

where ω_o is the angular frequency of the mains, and V_{rms} is the effective value of the output voltage.

By substituting L_1, L_2 and C into Equation (8), the resonant angular frequency ω_{res} is obtained.

$$\omega_{res} = \sqrt{\frac{L_1 + L_2}{L_1 L_2 C}} \tag{8}$$

In order to avoid the occurrence of resonance phenomenon, the capacitance and inductance values obtained must be substituted into Equation (9) to confirm whether the resonant angular frequency ω_{res} is within a reasonable range.

$$10\omega_o \leq \omega_{res} \leq \frac{1}{2}\omega_{sw} \tag{9}$$

where ω_{sw} is the angular frequency of the switch switching.

Finally, the passive damping resistor can be obtained by substituting the obtained L_t and C into Equation (10) [19].

$$R_d = \sqrt{\frac{L_t}{C}} \tag{10}$$

In this paper, the switching frequency of the switch is 20 kHz, the output sine wave frequency is 60 Hz, the output power is 1.6 kW, the output current ripple percentage is 5%, the amplitude modulation ratio is 0.9, the converter output voltage RMS is 220 V, and the DC-link voltage is 400 V. Therefore, the values of selected filter elements calculated by Equations (4)–(10) are L_1 = 12.86 mH, L_2 = 2.57 mH, C = 4 µF, and R_d = 23.1 Ω, and ω_{res} = 10,503.5 rad/s is within the reasonable range of Equation (9).

3.2. Inverter Output Voltage and Current Control

The control scheme of this system adopts the sinusoidal pulse-width modulation (SPWM) technique as the control basis, where the voltage and current control are added to the control process. The overall architecture of the control system is shown in Figure 5 [20].

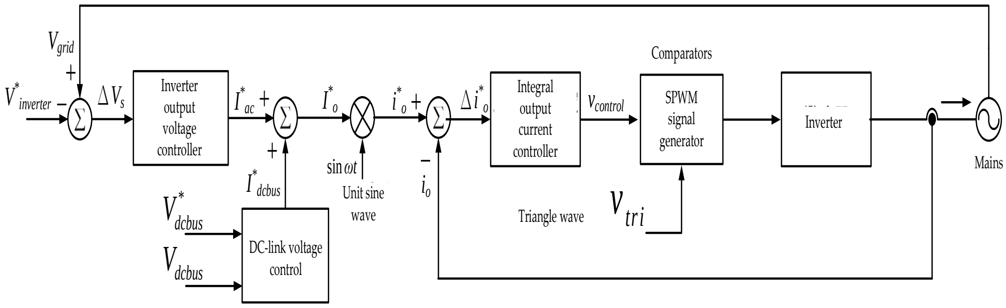

Figure 5. Control architecture of photovoltaic inverter output.

To make the inverter output voltage consistent with the mains voltage, after calculating the error between mains voltage V_{grid} and inverter output voltage $V^*_{inverter}$, the output current command I^*_{ac} of AC voltage controller was obtained via the P-I controller, and then added with the current command I^*_{dcbus} generated by the DC-link voltage control to obtain the output current command I^*_o of inner loop. This I^*_o was multiplied by the unit sine wave ($\sin \omega t$) at the same phase with a voltage of mains system connected in parallel to obtain the inverter output current command $i_o{}^*$. Consequently, a comparison with actual current i_o was conducted to obtain errors, where the control signal $v_{control}$ was received via the P-I controller. Lastly, $v_{control}$ was compared with the triangle carrier wave (v_{tri}) of fixed frequency to obtain the PWM control signal of the switch afterward, which allowed the inverter output current i_o to follow the current reference command i^*_o. This would allow the inverter output voltage to be consistent with the grid system voltage, and the inverter output voltage would be in the same phase as the current.

Figure 5 derives each control variable shown in Equations (11)–(14).

$$I^*_{ac} = K_{Pv}(V_{grid} - V^*_{inverter}) + K_{Iv}\int (V_{grid} - V^*_{inverter})dt \tag{11}$$

$$I^*_o = I^*_{ac} + I^*_{dcbus} \tag{12}$$

$$i_o^* = I_o^* \sin\theta \tag{13}$$

$$v_{control} = K_{Pi}(i_o^* - i_o) + K_{Ii}\int (i_o^* - i_o)dt \tag{14}$$

Among them, K_{Pv} = 0.1 and K_{Iv} = 5 were the proportional and integral constants of the P-I controller for the inverter output voltage. At the same time, K_{Pi} = 0.15 and K_{Ii} = 5 were the proportional and integral constants of the P-I controller for the inverter output current.

3.3. DC-Link Voltage Control

Since the insolation and the module temperature significantly affect the PVMA, the relationship between the output voltage and output current is nonlinear. Therefore, the characteristic curve also differs under different insolation and module temperature. For the photovoltaic system to reach maximum power output, the duty cycle for the power switch of the boost converter was controlled via MPPT, which kept the PVMA working at the MPP. Therefore, the output voltage of the boost converter was the unstable DC voltage, meaning the inverter input DC voltage was unstable. Therefore, to stabilize the inverter input DC voltage, the DC-link voltage at the inverter input must be controlled. Firstly, after acquiring the error between the DC-link V_{dcbus} voltage of the actual inverter input and the command voltage V_{dcbus}^* (400 V) that was set, the DC current command I_{dcbus}^* was then generated via the P-I controller. The control architecture of DC-link voltage is shown in Figure 6. When $V_{dcbus} > V_{dcbus}^*$, in order to stabilize the DC-link voltage at the reference command value (400 V), the DC-link voltage controller would raise the current command and increase the real power of inverter output; furthermore, the DC-link voltage was reduced for stabilization at the reference command value of DC-link voltage. When $V_{dcbus} < V_{dcbus}^*$, the DC-link voltage controller would reduce the current command value, so the DC-link voltage could raise to the voltage command value.

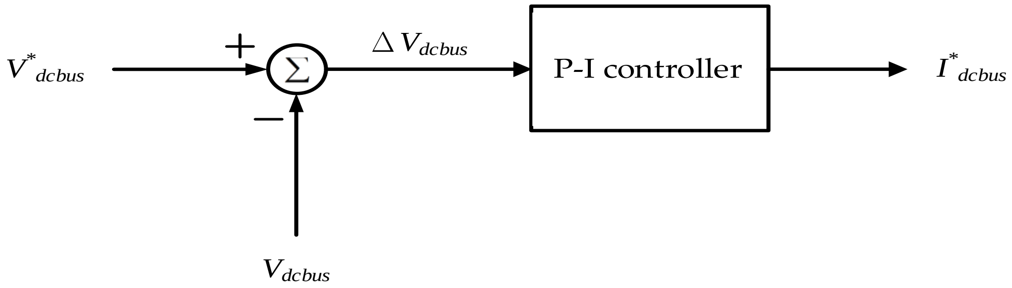

Figure 6. Control architecture of DC-link voltage.

From Figure 6, it is known that I_{dcbus}^* is expressed by the following formula:

$$I_{dcbus}^* = K_{Pdc}(V_{dcbus}^* - V_{dcbus}) + K_{Idc}\int (V_{dcbus}^* - V_{dcbus})dt \tag{15}$$

Among them, K_{Pdc} = 0.15 and K_{Idc} = 1 are the constants of the DC-link voltage P-I controller in this paper, respectively.

3.4. Output Power Control of a Three-Phase System

Reference [20] not only proposed the intelligent MPPT technology for PVMA but also engaged in the regulation of the output real power and reactive power of a single-phase smart inverter. However, the phase angle of the output voltage was detected by a sensor. The MPPT method of PVMAs is not the main focus of this paper. In this paper, we mainly regulate the output real power and reactive power of three-phase smart inverters to maintain the supply voltage of the grid system. To simplify the control complexity, we convert the coordinates of a three-phase to two-phase system of voltage, and estimate the phase angle of the grid voltage using the phase-locked loop (PLL) system based on the second-order generalized integrator (SOGI). Then, the estimated phase angle is substituted into Park's coordinate conversion matrix to convert the coordinates of the three-phase to two-phase voltage, so the installation of the phase sensor can be avoided.

Should the output of the grid-connected system for the three-phase inverter be a three-phase balanced system, the phases between the voltages or currents of the three-phase output differ by 120°. Generally, Park's transformation matrix [21,22] can be utilized to convert the *abc* axial vectors of the inverter into *dq* axial vectors for control. When analyzing the real and reactive powers of the three-phase system, the three-axial vector must also be converted into a two-axial vector DC system for calculation, which projects the *abc* three-phase stationary coordinates of the inverter to the $\alpha\beta$ stationary coordinates. The equation can be expressed as Equation (16).

$$T_{abc/\alpha\beta} = \frac{2}{3}\begin{bmatrix} 1 & \frac{-1}{2} & \frac{-1}{2} \\ 0 & \frac{\sqrt{3}}{2} & \frac{-\sqrt{3}}{2} \\ \frac{1}{2} & \frac{1}{2} & \frac{1}{2} \end{bmatrix} \tag{16}$$

Consequently, the $\alpha\beta$ stationary coordinates are converted to the *dq* synchronous rotating coordinates matrix. The equation can be expressed as Equation (17).

$$T_{\alpha\beta/dq} = \frac{2}{3}\begin{bmatrix} \cos\theta & \sin\theta & 0 \\ -\sin\theta & \cos\theta & 0 \\ 0 & 0 & 1 \end{bmatrix} \tag{17}$$

Among them, θ is the rotating angle of coordinates. Generally, θ is the phase of mains voltage, which makes the rotating angle of coordinates at the same phase as the mains voltage.

Based on Equations (16) and (17), it is known that the conversion matrix for converting *abc* three-phase stationary coordinates to *dq* synchronous rotating coordinates is shown in Equation (18).

$$T_{abc/dq} = \frac{2}{3}\begin{bmatrix} \cos\theta & \cos(\theta - \frac{2\pi}{3}) & \cos(\theta + \frac{2\pi}{3}) \\ -\sin\theta & -\sin(\theta - \frac{2\pi}{3}) & -\sin(\theta + \frac{2\pi}{3}) \\ \frac{1}{2} & \frac{1}{2} & \frac{1}{2} \end{bmatrix} \tag{18}$$

The block diagram for the phase estimation using a second-order generalized integrator (SOGI)-based phase-locked loop (PLL) system [23,24] is shown in Figure 7. Consequently, the phase estimated θ is fed back to the coordinate conversion matrix in Equation (18). Where the constants of the P-I controller were $K_{P\Theta}$ = 100 and $K_{I\Theta}$ = 50,000, respectively.

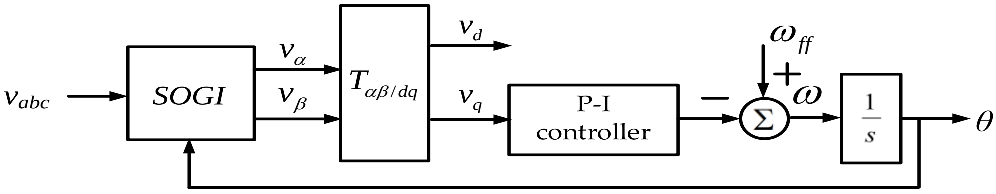

Figure 7. Block diagram for phase estimation using a SOGI-based PLL system.

After calculating the real and reactive power of inverter output, where errors were generated by comparing the command values of real power and reactive power, the direct axis current command I_d^* and quadrature axis current command I_q^* of the synchronous coordinates were obtained via the P-I controller. Consequently, the phase angle θ_{vi} difference between voltage and current could be calculated from Equation (19), where Figure 8 displayed the control architecture for the phase angle of a smart inverter [18]. In Figure 8, the proportional and integral constants of the P-I controller for real power were set as

K_{Pp} = 10 and K_{Ip} = 1, respectively, while the constants of the P-I controller for reactive power were set as K_{Pq} = 5 and K_{Iq} = 0.1, respectively.

$$\theta_{vi} = \tan^{-1}(\frac{I_q}{I_d}) \triangleq \theta_v - \theta_i \tag{19}$$

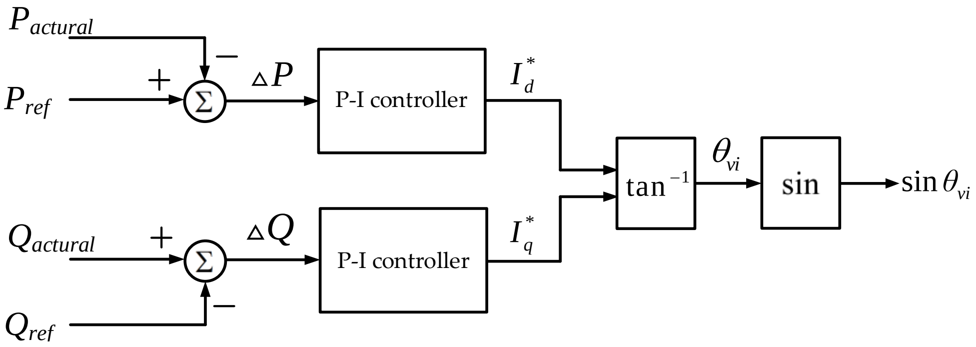

Figure 8. The control scheme for the phase angle of the smart inverter.

From the phase angle control for the smart inverter, the phase angle difference of grid voltage and current could be obtained θ_{vi}.

3.5. The Voltage-Power Control Technique for the Smart Inverter

When connecting the smart inverter to the mains system, the grid-connected specifications of the power company must be complied with. Since connecting a massive amount of renewable energy to the mains grid would cause voltage fluctuation, the voltage-power control technique must be applied, where attention is required to the allowable voltage scope in grid-connected specifications. When the photovoltaic smart inverter starts voltage-power control, should the mains voltage and frequency still fail in steady parallel operation and exceed the normal range, it must automatically trip to avoid damage.

Figure 9 displays the reactive power control architecture for the smart inverter [20]. The errors for actual mains voltage and reference voltage were acquired first; through the P-I controller (the proportional and integral constants were K_{Pg} = 0.1 and K_{Ig} = 0.13, respectively) and reactive power limiter, a command value of reactive power could be obtained. By entering the value in Figure 8, the smart inverter could be controlled to provide or absorb the reactive power for achieving the purpose of stabilizing mains voltage.

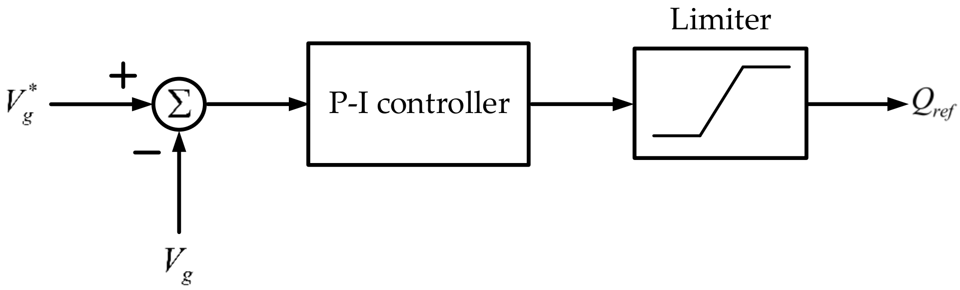

Figure 9. The reactive power control architecture for the smart inverter.

In order to be easy to implement, all the controllers in this paper adopt the traditional proportional-integral (P-I) controller, whose proportion and integral constant are obtained by the "trial and error" method.

Figure 10 shows the voltage-power control flow chart [20]. Firstly, the voltage at the grid-connected point of the inverter is detected to control the reactive power according to the per-unit value of mains voltage. When such value equals 1, the power factor (PF) also stays at 1. Since no reactive power occurs then, only the provision of real power is required. When the per-unit value of mains voltage is between 1 p.u.~1.03 p.u., the smart inverter will absorb the reactive power, where PF is controlled and gradually reduces to 0.9 (lagging). When the per-unit value of mains voltage is between 0.97 p.u. and 1 p.u., the smart inverter will provide the reactive power, where PF is controlled and gradually reduces to 0.9 (leading). The above control brings the mains voltage back to the normal range by adjusting the magnitude of the reactive power. However, should PF be adjusted to 0.9 leading or lagging and the mains voltage still cannot effectively restrain its rise or fall, the "technical highlights for parallel connection of renewable energy power generation system, Taiwan Power Company" [25] will be followed. When the voltage is greater than 1.03 p.u. or less than 0.97 p.u., the smart inverter will be disconnected from the mains system.

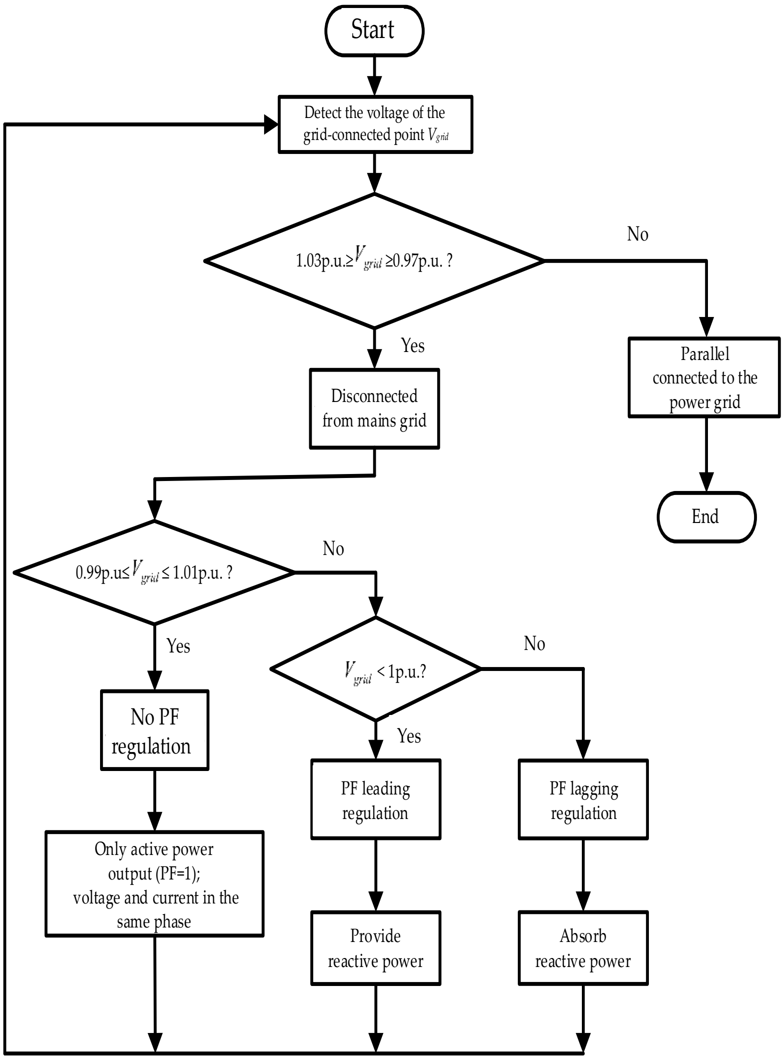

Figure 10. Voltage-power control flow chart.

4. Simulation Results

The three-phase photovoltaic smart inverter could provide or absorb the reactive power of the mains system and achieve the purpose of stabilizing the mains voltage. To verify that the control architecture mentioned in this paper was applicable for a common load in the market, the inductive load was selected for the actual test. Tables 1 and 2 displayed the electrical parameters of the boost converter (in Figure 3) and inverter (in Figure 4), respectively. In this paper, the KYOCERA KC200GT photovoltaic modules

(PVMS) were connected in four serials and two parallels to construct a 1600 W PVMA. The electrical specifications of the PVM are shown in Table 3.

Table 1. The electrical parameters of the boost converter.

Electrical Parameter	Specifications
Range of input voltage (V_{in})	90~108 V
Inductance (L)	0.5 mH
Output capacitor (C_{out})	470 µF/450 V_{DC}
Output voltage (V_{out})	400 V
Switch frequency of boost converter (f)	20 kHz

Table 2. Electrical parameter of inverter.

Electrical Parameter	Specifications
DC-link capacitor (C_{dcbus})	1000 µF/450 V_{DC}
DC-link voltage (V_{dcbus})	400 V
Filter inductance ($L_{1\ a,b,c}$)	12.86 mH
Filter inductance ($L_{2\ a,b,c}$)	2.57 mH
Filter capacitor ($C_{\ a,b,c}$)	4 µF/400 V_{AC}
AC voltage ($V_{grid\ a,b,c}$)	220 V_{rms}
Switch frequency of SPWM (f_{tri})	20 kHz

Table 3. Electrical specifications of KYOCERA KC200GT PVMA.

Electrical Parameter	Specifications
Open circuit voltage (V_{oc})	131.6 V
Short circuit current (I_{sc})	16.42 A
Maximum output power point voltage (V_{pm})	105.2 V
Maximum output power point current (I_{pm})	15.22 A
Rated maximum output power (P_{max})	1600 W

4.1. Simulation Results of the Smart Inverter Control

The architecture of a three-phase photovoltaic smart inverter system built with PLECS software split the tested mains into three types of voltage range: (1) $V_{grid} = 1$ p.u.; (2) 1.03 p.u. $> V_{grid} \geq 1$ p.u.; and (3) 1 p.u. $> V_{grid} > 0.97$ p.u. The smart inverter control was utilized for providing or absorbing reactive power, which further regulated the mains voltage.

4.1.1. The Per-Unit Value of the Mains Voltage Equals 1 p.u.

When the per-unit value of mains voltage detected was 1 p.u., the PF of the photovoltaic smart inverter stayed at 1. The simulation result is shown in Figure 11. Figure 11 also displayed the output power of the smart inverter when the per-unit value of mains voltage equaled 1 p.u. From Figure 11, it could be observed that the PV system only provided real power to the mains. The reactive power was neither provided nor absorbed. Figure 12, by contrast, displayed the output voltage and current waveforms of the mains and smart inverter. From Figure 12, it could be observed that the output voltage and current were in a three-phase balance and the same phase.

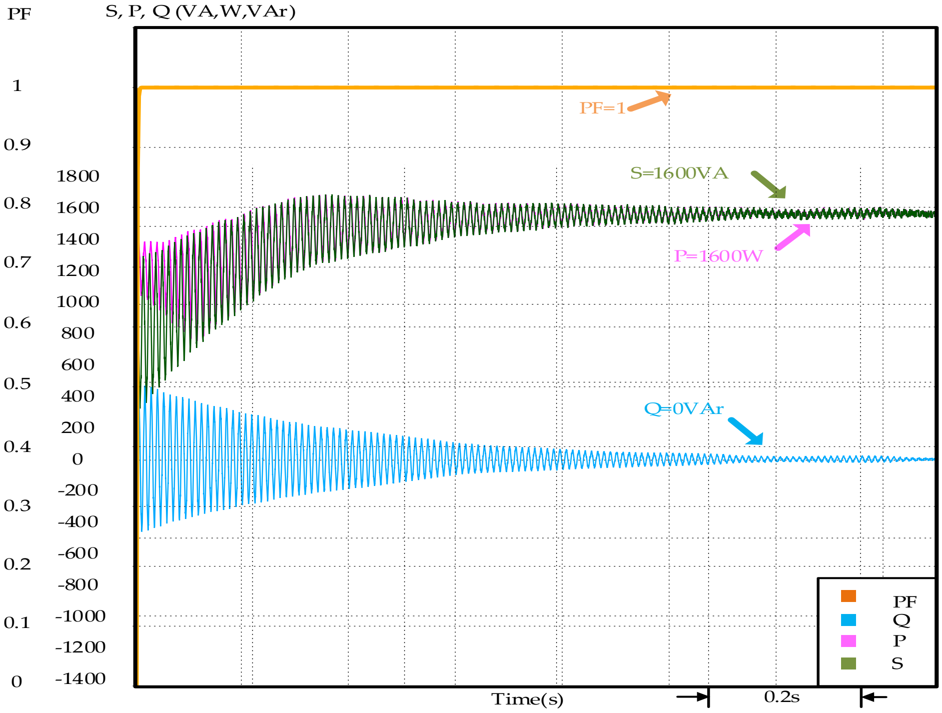

Figure 11. The output PF, real power, reactive power, and apparent power of the smart inverter when the per-unit value of mains voltage equals 1 p.u.

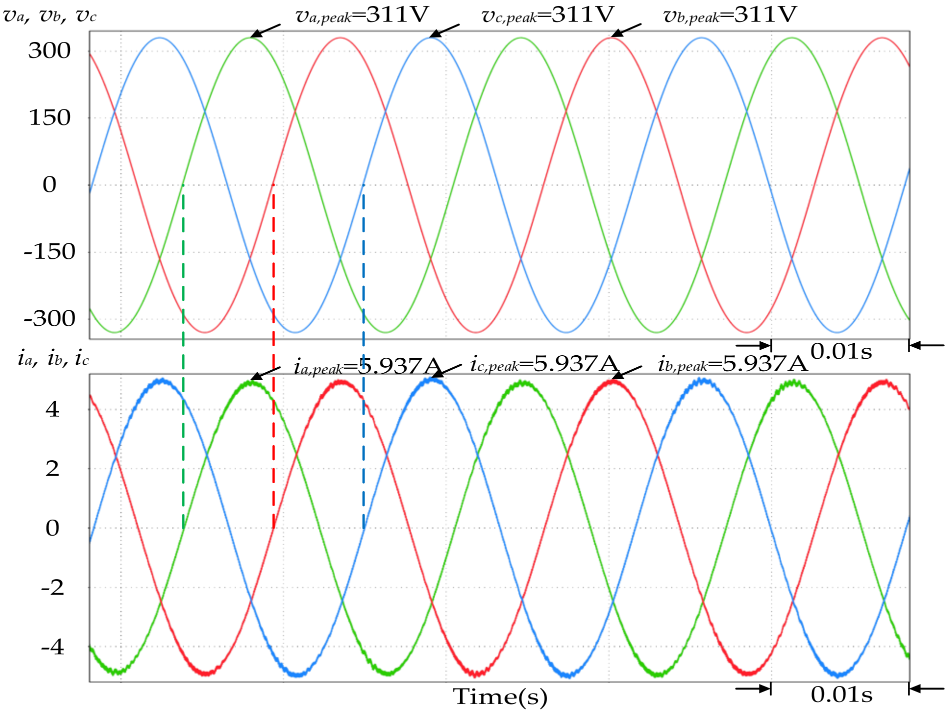

Figure 12. The three-phase output voltage and current waveforms of the smart inverter when the per-unit value of mains voltage equals 1 p.u.

4.1.2. Per-Unit Value of the Mains Voltage Was between 1 p.u. and 1.03 p.u.

When more renewable energy connects to the mains, the power of the grid-connected photovoltaic system feeding into the mains would also rise. This would cause the mains voltage to rise and appliance damage at the user end. Therefore, when the per-unit value of mains voltage detected by the system was between 1 p.u.~1.03 p.u., the smart inverter should start to be controlled to absorb the reactive power of the system. From Figure 13, it could be observed that when the photovoltaic system fed excessive power to the mains, the mains voltage V_{grid} would gradually increase if not regulated. However, should regulation be conducted with the voltage-power control technique of the photovoltaic smart inverter mentioned, the mains voltage V_{grid} would reduce to the root-mean-square value of 220 V (1 p.u.). Therefore, the increase in mains voltage could be inhibited. As shown in Figure 13, the PF of the smart inverter was adjusted to 0.9 (lagging) to absorb the redundant reactive power. Figure 13, by conrast, also displayed the output power of the smart inverter when the per-unit value of mains voltage was between 1 p.u. and 1.03 p.u. It could be observed that the reactive power of mains absorbed by the inverter was 774 VAr ($Q > 0$); then, the apparent power S still remained at 1600 VA as the apparent output power of PVMA, while the output real power P of the smart inverter reduced to 1440 W. Figure 14 displayed the three-phase output voltage and current waveforms of the smart inverter when the per-unit value of mains voltage was between 1 p.u. and 1.03 p.u. From Figure 14, the three-phase balance could be observed, but the current was lagging behind voltage; thus, the PF was lagging.

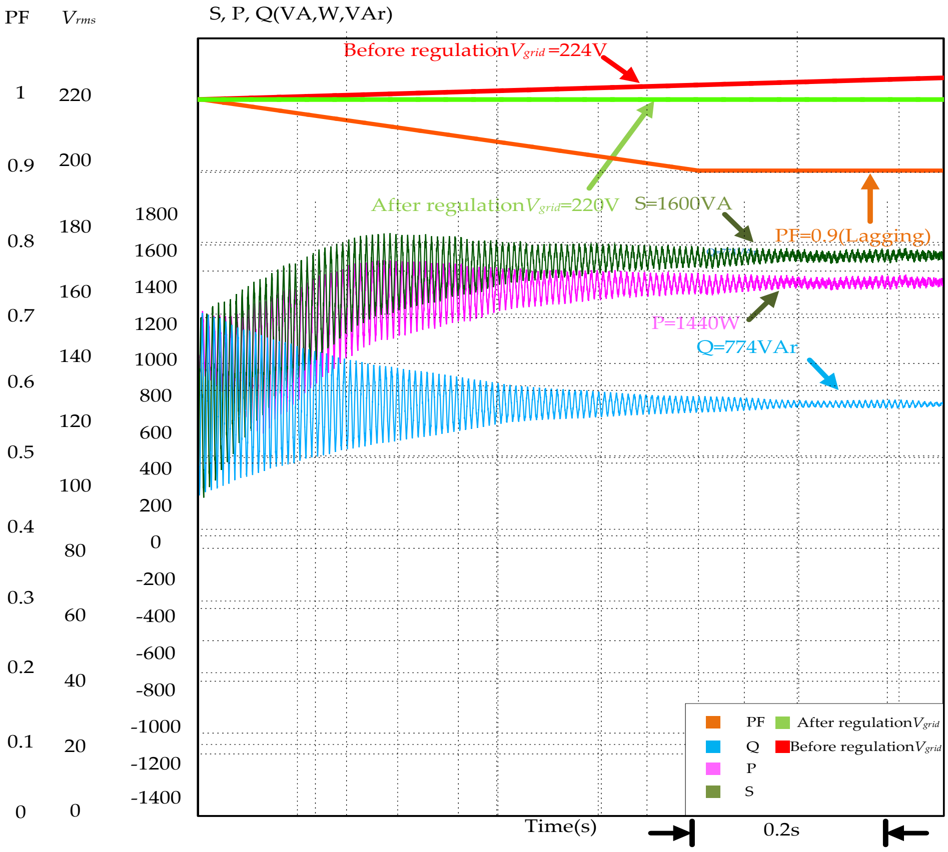

Figure 13. The mains voltage V_{grid} before and after regulation, output PF regulation, real power, reactive power, and apparent power of the smart inverter when the per-unit value of mains voltage was between 1 p.u. and 1.03 p.u.

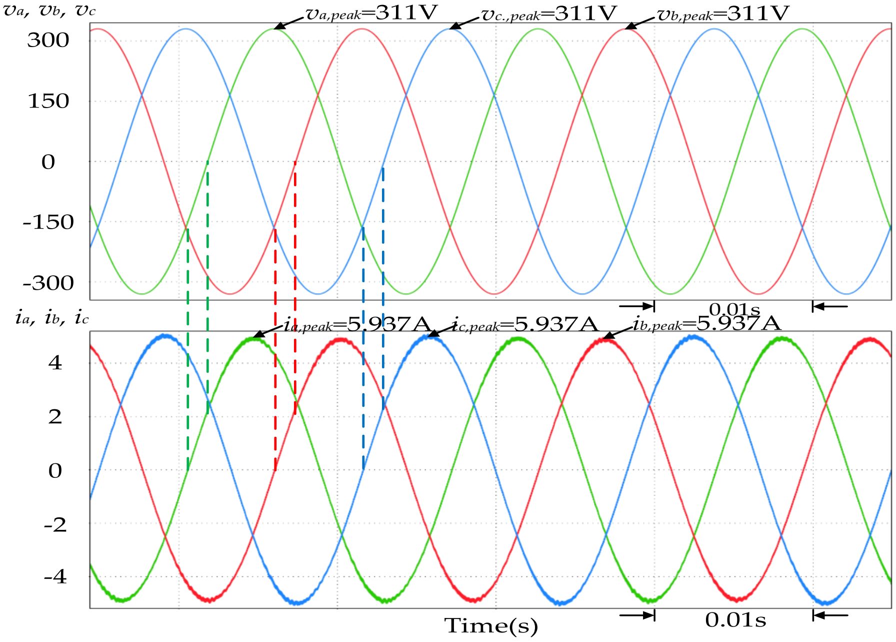

Figure 14. The three-phase output voltage and current waveforms of the smart inverter when the per-unit value of mains voltage was between 1 p.u. and 1.03 p.u.

4.1.3. Per-Unit Value of Mains Voltage Was between 0.97 p.u. and 1 p.u.

Environmental factors, such as poor weather or shades from objects, would cause reduced power generation of the photovoltaic power generation system, which leads to the voltage of the grid-connected point less than 1 p.u. and easily causes appliance damage at the load end. Therefore, the mains voltage must be increased. Hence, when the per-unit value of mains voltage detected was between 0.97 p.u.~1 p.u., the photovoltaic smart inverter would start the control for supplying reactive power. From Figure 15, it could be observed that in the case of a sudden reduction in mains power fed from the photovoltaic system, the mains voltage V_{grid} would reduce gradually if not regulated. However, should regulation be conducted with the voltage-power control technique of the photovoltaic smart inverter mentioned, the mains voltage V_{grid} would increase to the root-mean-square value of 220 V (1 p.u.), which would maintain the mains voltage at a stable value. From Figure 15, it could be also observed that the PF of the smart inverter was adjusted to 0.9 (leading); thus, the reactive power could be provided to the mains. Figure 15, by contrast, also displayed that the output power of the smart inverter when the per-unit value of mains voltage was between 0.97 p.u. and 1 p.u. From Figure 15, it could be observed that the inverter provided reactive power of 774 VAr ($Q < 0$) to the mains, the output apparent power S for the inverter still maintained output capacity of the 160 A as for the PVMA, and the output real power P of the smart inverter reduced to 1440 W. Figure 16 displayed the three-phase output voltage and current waveforms of the smart inverter when the per-unit value of mains voltage was between 0.97 p.u. and 1 p.u. From Figure 16, it could be observed that the three-phase balance was still maintained, and then, the current was leading ahead of the voltage; thus, the PF was leading.

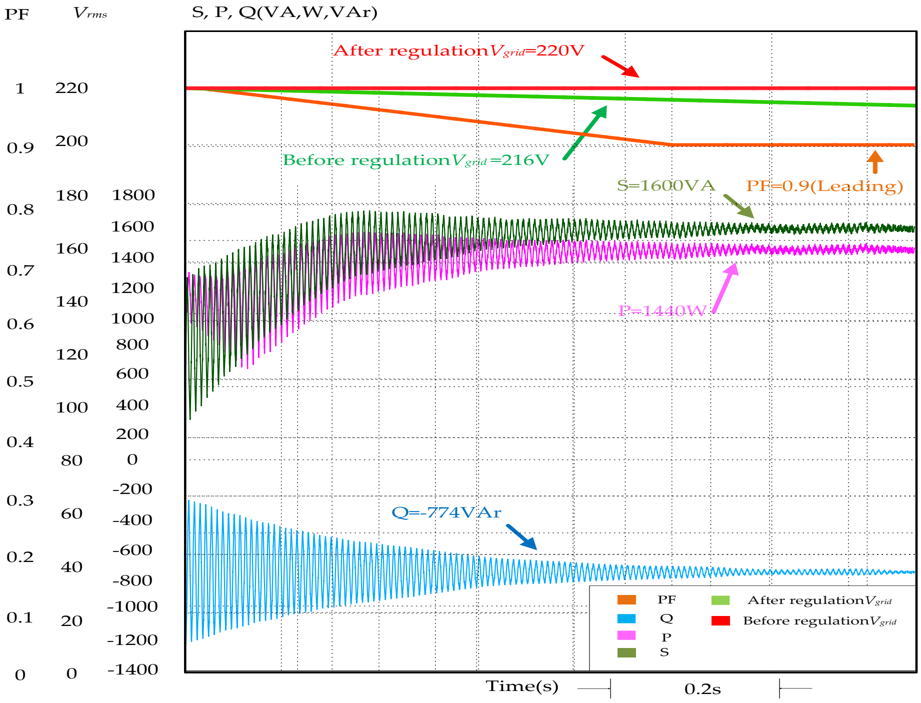

Figure 15. The mains voltage V_{grid} before and after regulation, the output PF regulation, real power, reactive power, and apparent power of the smart inverter when the per-unit value of mains voltage was between 0.97 p.u. and 1 p.u.

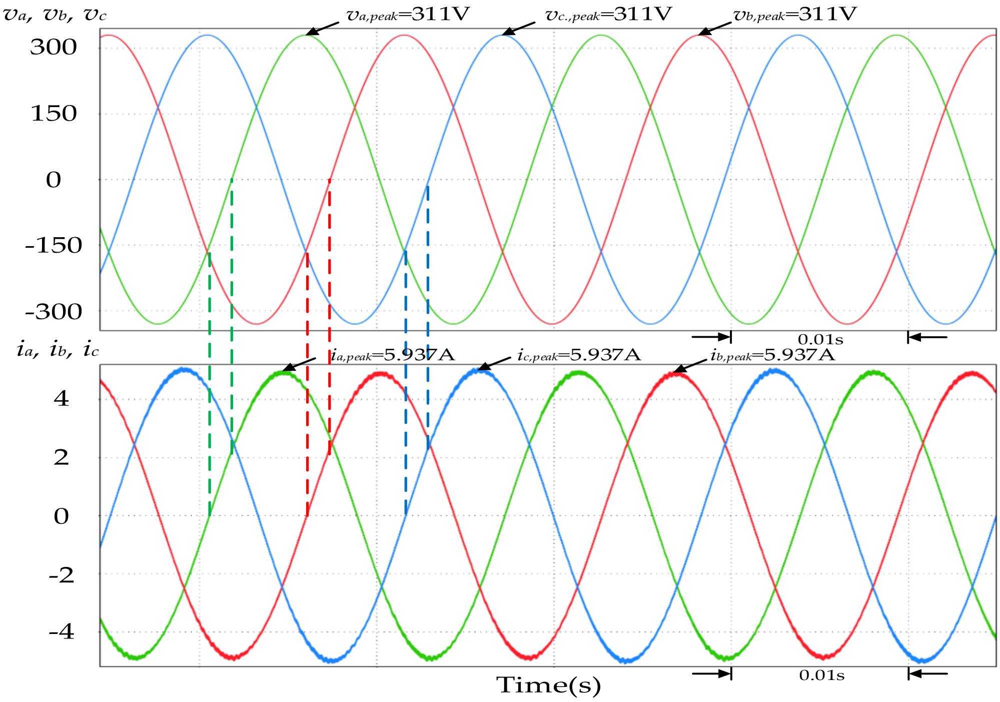

Figure 16. The three-phase output voltage and current waveforms of the smart inverter when the per-unit value of mains voltage was between 0.97 p.u. and 1 p.u.

4.2. Results of Actual Test for Smart Inverter Control

In this paper, the multifunction (circuit and control) simulation software PLECS system developed by Swiss Company Plexim GmbH combined with RT box as an actual test simulation controller and analog breakout board for test simulation to finish the actual control test on the smart inverter.

Usually, when no abnormal fluctuation occurs at the voltage of a PV grid-connected system, the photovoltaic inverter generally controls both the output voltage and current under sine wave and the same phase, so the output PF becomes 1.0. Therefore, all the output power of the photovoltaic system can be connected and sent to the grid by means of real power. In the case of a sudden increase or reduction in insolation, the power of the grid-connected system fed from the grid-connected photovoltaic system would also experience a sudden increase or reduction. The same would occur in the voltage at the grid-connected point if the load end could not consume or refill if the voltage suddenly increased or reduced, which would cause damage to equipment at the load end. To avoid such a situation, the real and reactive power were regulated via a smart inverter for stabilizing the voltage at the grid-connected point. The per-unit value of the voltage of the grid-connected point was between 1.0 p.u. and 1.03 p.u., which meant that the reactive power of the grid system was negative ($Q < 0$), which made the leading PF of the grid system. Therefore, the output current of the smart inverter should be controlled to be lagging behind the voltage, so the PF was lagging, where the reactive power of the grid system could be absorbed to stabilize the voltage at the grid-connected point.

Figure 17a,b displayed the three-phase balanced output voltage and current waveforms under the actual test of the smart inverter, while Figure 18a,b displayed the output voltage and current waveforms under the actual test of the smart inverter under Phase a and the waveforms after partial enlargement, respectively. From Figure 18b, it could be observed that when the per-unit value of the voltage of the grid-connected point was between 1.0 p.u. and 1.03 p.u., the smart inverter started to control the output current, the phase was lagging behind the output voltage and the PF was adjusted to be lagging for absorbing reactive power of the grid system. From the output power regulation under the actual test of the smart inverter in Figure 19, it could be observed that through the PF regulation of the smart inverter, the real power in the grid fed from the inverter reduced from 1600 W to 1440 W and absorbed the reactive power of 774 VAr ($Q > 0$) in grid system. However, the total output of apparent power is still maintained at the PVMA capacity of 1600 VA.

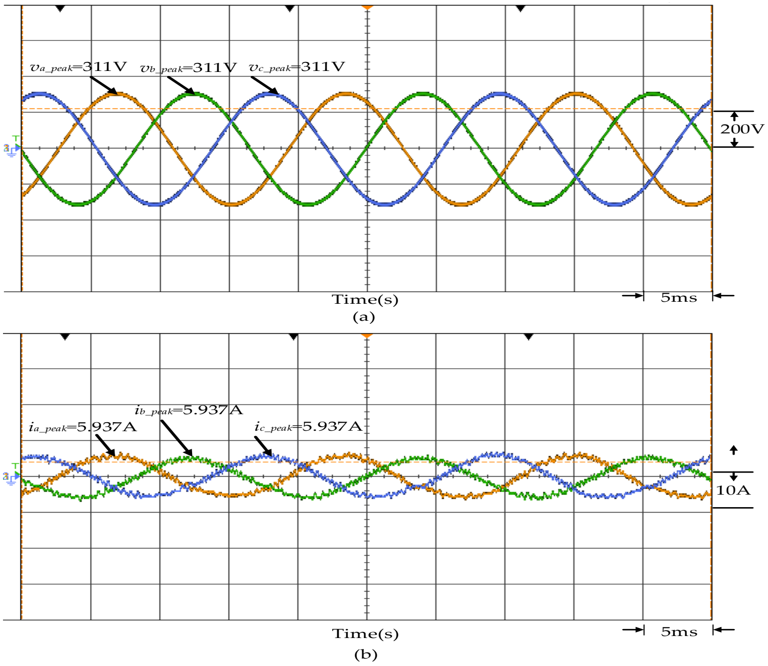

Figure 17. The three waveforms under the actual test of the smart three-phase inverter: (**a**) output voltage waveforms; (**b**) output current waveforms.

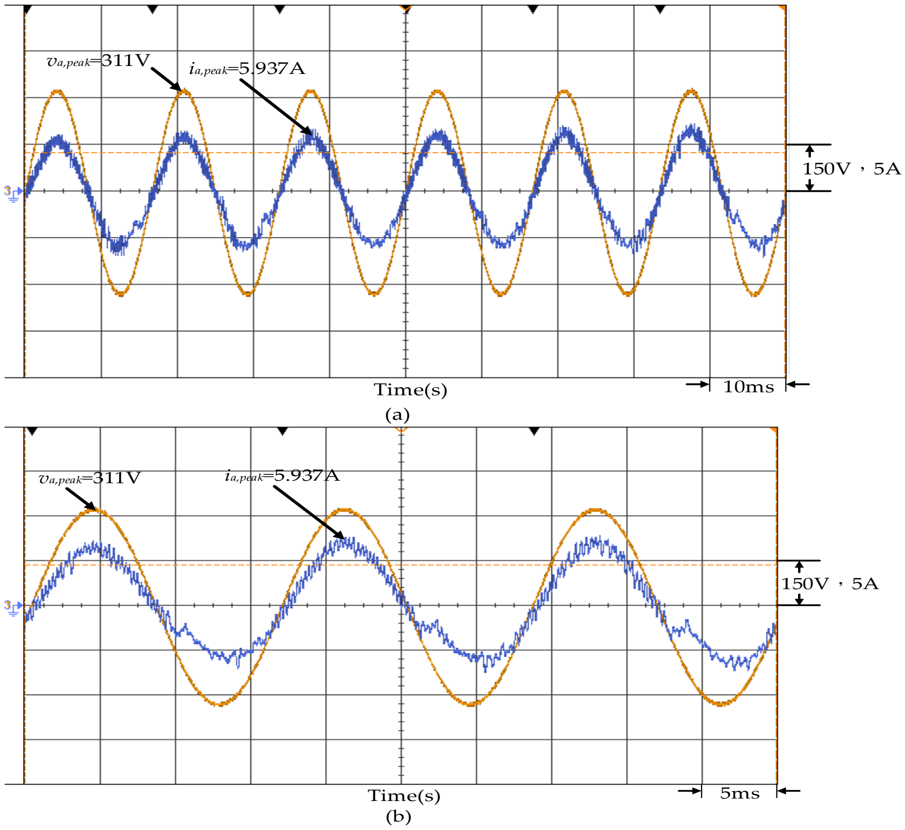

Figure 18. When the per-unit value of mains voltage in smart inverter under Phase a was between 1 p.u. and 1.03 p.u.: (**a**) output voltage and current waveforms under the actual test; (**b**) partial waveform enlargement of Figure (**a**).

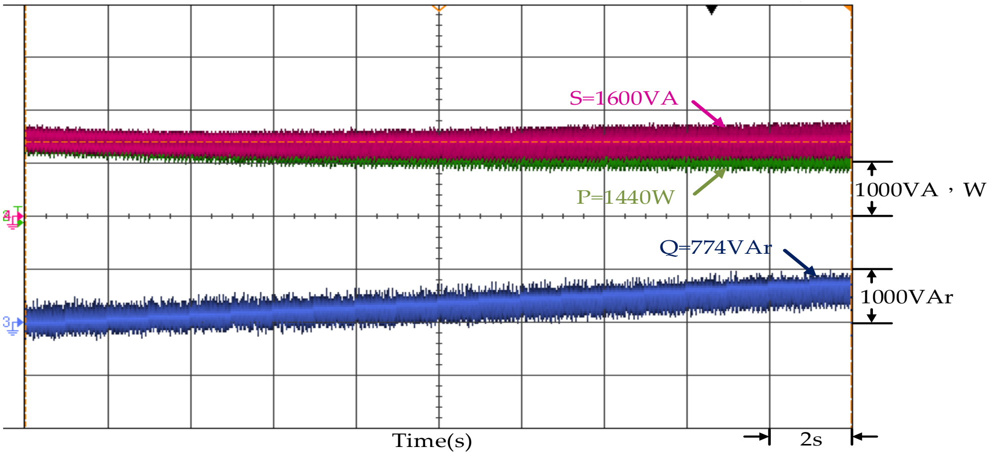

Figure 19. The output power regulation of the smart inverter when the per-unit value of mains voltage was between 1 p.u. and 1.03 p.u.

As the current waveform in Figure 18 is the waveform obtained by actual measurement, the current signal is converted into a voltage signal by the current detector and then measured. To avoid the high switching frequency of the power semiconductor switch, the switch will be overheated and burned due to high switching loss. Therefore, the actual current control adopts hysteresis current control. The measured current switched control within the current width set by the current command's upper limit and lower limit. Moreover, under the high-frequency switching control of the switch, the measurement is susceptible to high-frequency signal interference, resulting in the distortion of the measured current signal in Figure 18. The distortion of the current signal will also cause the distortion of the measured observed apparent power, real power, and reactive power signal in Figure 19.

When the PVMA encountered a sudden drop in power generation due to the influence of unexpected shades from clouds or other climate factors, which set the per-unit value of the voltage of the grid-connected point between 0.97 p.u. and 1.0 p.u., the reactive power of the grid system was positive (Q > 0) and PF of the system was lagging. Therefore, the output current of the smart inverter should be controlled to be leading ahead of the output voltage, so the PF was leading, where the reactive power of the grid system could be provided to stabilize the voltage at the grid-connected point. Figure 20a,b displayed the output voltage and current waveforms under the actual test of the smart inverter under Phase a and the waveforms after partial enlargement, respectively. From Figure 20b, it could be observed that when the per-unit value of the voltage of the grid-connected point was between 0.97 p.u. and 1.0 p.u., the smart inverter started to control the output current, the phase was leading ahead of the output voltage, and the PF was adjusted to be leading for providing reactive power of the system. From the output power alteration under the actual test of the smart inverter in Figure 21, it was known that through the PF regulation of the smart inverter, the real power in grid fed from the inverter reduced from 1600 W to 1440 W but provided the reactive power of 774 VAr (Q < 0) to grid system. However, the total output of apparent power still maintained at the PVMA capacity of 1600 VA.

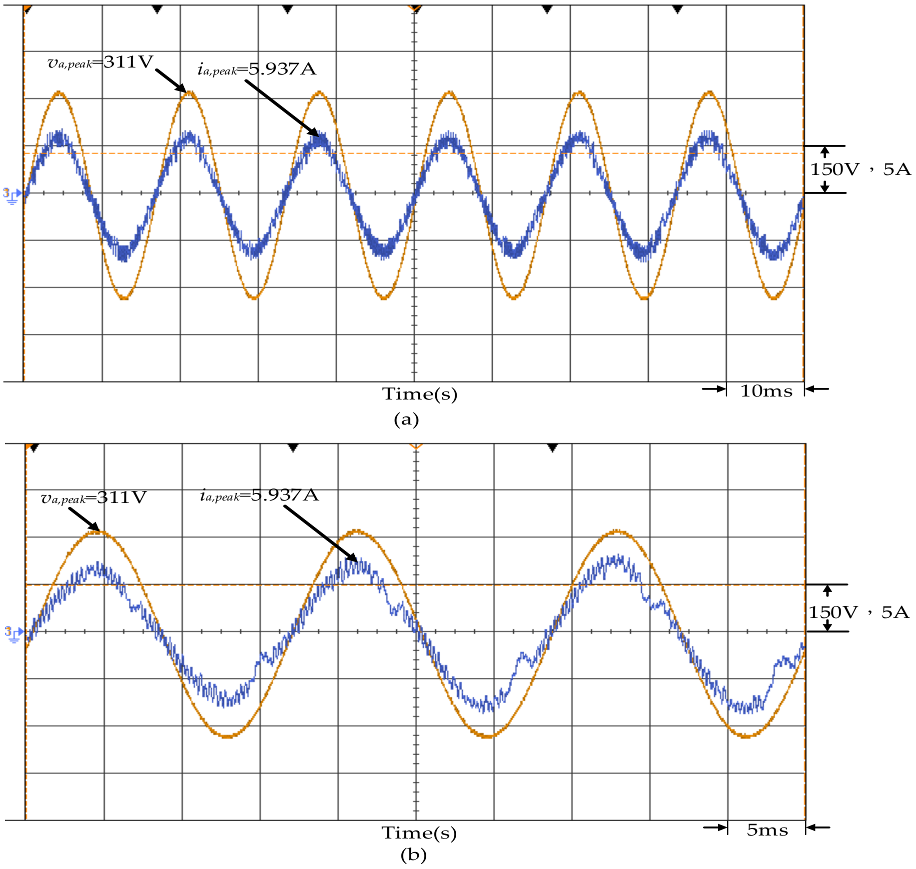

Figure 20. When the per-unit value of mains voltage in smart inverter under Phase a was between 0.97 p.u. and 1 p.u.: (**a**) output voltage and current waveforms under the actual test; (**b**) partial waveform enlargement of Figure (**a**).

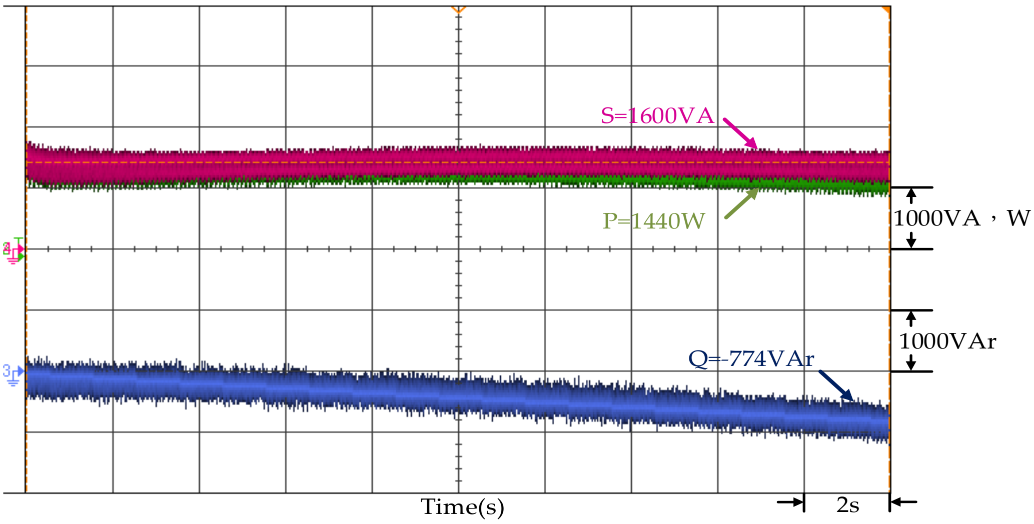

Figure 21. The output power regulation of the smart inverter when the per-unit value of mains voltage was between 0.97 p.u. and 1 p.u.

Through results from the simulation and an actual test, it was verified that the developed photovoltaic smart inverter could provide or absorb reactive power for the grid system by controlling PF at the output end, so the voltage of the grid system could be stabilized. Therefore, the developed smart inverter in this paper is feasible and applicable.

The test results of the three cases are summarized in Table 4. It can be seen from Table 4 that the converter can adjust the power factor (PF) at the end of the grid system by adjusting the output real power and reactive power, so that under the fixed output power of photovoltaic system, regardless of the increased or decreased system load, the grid system voltage of the parallel point can be controlled to a fixed value. Still, the output apparent power remains unchanged, that is, the same as the maximum output power of the PVMA.

Table 4. Test results of three cases of smart inverter.

Case	**PF**		**V_{grid} (V)**		**S (VA)**		**P (W)**		**Q (VAr)**	
	Before Regulation	**After Regulation**	**Before Regulation**	**After Regulation**	**Before Regulation**	**After Regulation**	**Before Regulation**	**After Regulation**	**Before Regulation**	**After Regulation**
1	1.0	1.0	220	220	1600	1600	1600	1600	0	0
2	1.0~1.03	0.9 (lagging)	240	220	1600	1600	1600	1440	0	774
3	0.97~1.0	0.9 (leading)	216	220	1600	1600	1600	1440	0	−774

Since the power generation of the photovoltaic system is mainly to assist the power grid system in supplying power to the load, the power supply ratio is not large. Only when the load suddenly plummets and causes the voltage of the load terminal to rise sharply, the real power output of the smart inverter can be lowered and the reactive power absorbed by the smarter inverter can be increased while the power output of the photovoltaic system remains unchanged. The load terminal voltage is controlled to maintain the rated voltage to ensure the power supply quality of the power system. The simulation and actual test results under this condition have been verified in this paper. As for the small amounts of sunlight due to the reduction in the photovoltaic system, the smart inverter will control the total output to the real power to assist the power grid for power supply. However, when the load is too high, the voltage drop of the power grid system is too large. If the total output power of the photovoltaic system is controlled by the smart inverter to real power, but the voltage of the power grid system still cannot be maintained, the power grid system must be cut off to avoid disasters.

Unlike the conventional smart inverter architecture, the phase-locked loop (PLL) system based on the second-order generalized integrator (SOGI) is used to estimate the phase angle of the grid voltage. Then, the estimated phase angle is substituted into Park's coordinate conversion matrix to implement the coordinate conversion of the three-phase to the two-phase voltage, which can be dispensed with the installation of a phase angle sensor. In addition, the proportional-integral controller commonly used in the industry controls the DC-link voltage, the real power, and reactive power of the inverter. Although its control performance is less robust than that of an intelligent controller, it can shorten the operation time of the controller and improve the response speed. It is worth mentioning that PLECS, a multifunctional simulation software of power electronic real-time control system of the integrated circuit and control system developed by Plexim GmbH in Switzerland, is used in this paper. At the same time, the simulation and measured environment of three-phase mains in a grid-connected photovoltaic power generation system are established. Combined with the actual test of the analog controller RT Box and analog line splitter board—analog breakout board, the control measurement of the smart inverter was completed. Therefore, the verification between simulation and actual measurement could be completed quickly, and the development time of the smart inverter could be shortened.

5. Conclusions

This paper primarily discussed the design and development of a three-phase grid-connected photovoltaic smart inverter. The design of circuit architecture mainly consists of the boost converter and three-phase full-bridge inverter. The multifunction simulation software PLECS was applied to connect the photovoltaic modules KC200GT as four in series and two in parallel to form a PVMA of 1600 W, which combined the RT box and analog breakout board of PLECS to conduct an actual test on the three-phase photovoltaic grid-connected smart inverter. For the control of the photovoltaic smart inverter, the simple P-I controller was adopted in this paper to control the DC-link voltage at 400 V. Additionally, the developed smart inverter can regulate the grid voltage at 1.0 p.u. value (root-mean-square value is 220 V) by adjusting its output reactive power when the grid voltage p.u. value is higher or lower than 1.0. However, when the grid voltage is higher than 1.03 p.u. or less than 0.97 p.u., the grid voltage does not conform to the power specification, so it cannot maintain the grid voltage at norminal value by adjusting the reactive power of the smart inverter. At this point, the protection equipment will act to cut off the load from the power system to avoid greater disasters. From the results of the simulation and actual test, it proves that the photovoltaic smart inverter developed in this paper can connect with the mains system. Through the voltage-power regulation, the smart inverter can absorb or provide reactive power in the mains, where the voltage quality of the mains supply is improved further.

Author Contributions: K.-H.C. planned the project and did the writing, editing and review. K.-H.C. also evaluated the performance of the whole smart inverter system. K.-H.H. was responsible for designing the whole system structure and developing the smart inverter. Z.-Y.S., completed the simulation and exteriments of V-P control of the smart photovoltaic grid-connected inverter to improve the power quality of the grid system. C.-Y.H. accomplished the data curation, soft program, and validation for the P&O MPPT controller. K.-H.C., administered the project. All authors have read and agreed to the published version of the manuscript.

Funding: The authors gratefully acknowledge the support and funding of this project by Ministry of Science and Technology, Taiwan, under the Grant Number MOST 110-2221-E-167-007-MY2.

Institutional Review Board Statement: Not applicable.

Informed Consent Statement: Not applicable.

Data Availability Statement: This study did not report any data.

Conflicts of Interest: The authors of the manuscript declare no conflict of interest.

References

1. Gupta, S.; Kekatos, V.; Jin, M. Controlling Smart Inverters Using Proxies: A Chance-constrained DNN-based Approach. *IEEE Trans. Smart Grid* **2022**, *13*, 1310–1321. [CrossRef]
2. Gush, T.; Kim, C.H.; Admasie, S.; Kim, J.S.; Song, J.S. Optimal Smart Inverter Control for PV and BESS to Improve PV Hosting 655 Capacity of Distribution Networks Using Slime Mould Algorithm. *IEEE Access* **2021**, *9*, 52164–52176. [CrossRef]
3. Chavali, R.; Dey, A.; Das, B. Grid Connected Three-level VSI Based Smart Solar Inverter Using Online Space Vector Based Hysteresis Current Control. In Proceedings of the IEEE International Conference on Power Electronics, Smart Grid and Renewable Energy, Cochin, India, 2–4 January 2020; pp. 1–6.
4. PLECS Website, Plexim Electrical Engineering Software. Available online: https://www.plexim.com/products/plecs (accessed on 17 June 2022).
5. KC200GT Data Sheet, Kyocera. Available online: https://www.energymatters.com.au/images/kyocera/KC200GT.pdf (accessed on 5 June 2022).
6. Verma, R.; Ansari, M.A. Photovoltaic Power Efficient Adjustment Using Maximum Power Point Tracking and Boost Converter. In Proceedings of the 4th International Conference on Recent Developments in Control, Automation & Power Engineering, Noida, India, 7–8 October 2021; pp. 43–46.
7. Nkambule, M.S.; Hasan, A.N.; Ali, A. MPPT under Partial Shading Conditions Based on Perturb & Observe and Incremental Conductance. In Proceedings of the 11th International Conference on Electrical and Electronics Engineering, Bursa, Turkey, 28–30 November 2019; pp. 85–90.
8. Rao, C.V.R.; Ganesh, M.S.R.; Sekhar, K.C.; Sudha, R.P.; Dangeti, L.K.; Duvvuri, S.S.S.R.S. A Generalized MPPT Controlled DC-DC Boost Converter for PV System Connected to Utility Grid. In Proceedings of the Innovations in Power and Advanced Computing Technologies, Vellore, India, 22–23 March 2019; pp. 1–5.
9. Balal, A.; Shahabi, F. Ltspice Analysis of Double-inductor Quadratic Boost Converter in Comparison with Quadratic Boost and Double Cascaded Boost Converter. In Proceedings of the 12th International Conference on Computing Communication and Networking Technologies, Kharagpur, India, 6–8 July 2021; pp. 1–6.
10. Hart, D.W. *Power Electronics*, 1st ed.; Mcgraw Hill Higher Education: New York, NY, USA, 2011.
11. Li, Y.; Ang, K.H.; Chong, G.C.Y. Patents, Software, and Hardware for PID Control: An Overview and Analysis of the Current Art. *IEEE Contr. Syst. Magaz.* **2006**, *26*, 42–54.
12. Ghanayem, H.; Alathamneh, M.; Nelms, R.M. A Comparative Study of PMSM Torque Control Using Proportional-integral and Proportional-resonant Controllers. In Proceedings of the Southeast Conference, Mobile, AL, USA, 26 March–3 April 2022; pp. 453–458.
13. Oh, J.; Kim, J.-H.; Lee, J.; Jung, E.K.; Oh, D.; Min, J.; Im, H.; Kim, I.S. Pixel Circuit with P-type Low-temperature Polycrystalline Silicon Thin-film Transistor for Micro Light-emitting Diode Displays using Pulse Width Modulation. *IEEE Electron. Device Lett.* **2021**, *42*, 1496–1499. [CrossRef]
14. Mahbub, M.; Hossain, M.A. Design Simulation and Comparison of Three-phase Symmetrical Hybrid Sinusoidal PWM Fed Inverter with Different PWM Techniques. In Proceedings of the 2nd International Conference on Robotics, Electrical and Signal Processing Techniques, Dhaka, Bangladesh, 5–7 January 2021; pp. 1–5.
15. Zhao, T.; Shen, W.J.; Ji, N.Y.; Liu, H.H. Study and Implementation of SPWM Microstepping Controller for Stepper Motor. In Proceedings of the 13th IEEE Conference on Industrial Electronics and Applications, Wuhan, China, 31 May–2 June 2018; pp. 2298–2302.
16. Cha, H.; Vu, T. Comparative Analysis of Low-pass Output Filter for Single-phase Grid-connected Photovoltaic Inverter. In Proceedings of the 25th Annual IEEE Applied Power Electronics Conference and Exposition, Palm Springs, CA, USA, 21–25 February 2010; pp. 1659–1665.
17. Zhang, Y.; Zhou, X.; Chen, Y.; Lu, S. Three-phase Four-wire LCL Filter Active Damping Control Based on Common Mode Capacitor Current Feedback. In Proceedings of the 6th International Conference on Power and Renewable Energy, Shanghai, China, 17–20 September 2021; pp. 328–332.
18. Liu, F.; Zha, X.; Zhou, Y.; Duan, S. Design and Research on Parameter of LCL Filter in Three-phase Grid-connected Inverter. In Proceedings of the IEEE 6th International Power Electronics and Motion Control Conference, Wuhan, China, 17–20 May 2009; pp. 2174–2177.
19. Channegowda, P.; John, V. Filter Optimization for Grid Interactive Voltage Source Inverters. *IEEE Trans. Ind. Electron.* **2010**, *57*, 4106–4114. [CrossRef]
20. Huang, K.H.; Chao, K.H.; Sun, Z.Y.; Liao, Y.H. Online Control of Smart Inverter for Photovoltaic Power Generation Systems in a Smart Grid. *Front. Energy Res.* **2022**, *10*, 879385. [CrossRef]
21. Krause, P.C.; Wasynczuk, O.; Sudhoff, S.D. *Analysis of Electric Machinery and Drive Systems*, 2nd ed.; Wiley-IEEE Press: New York, NY, USA, 2002.
22. Chen, C.; Chen, Y.; Yang, X.; Gao, S.; Zhang, B. Inverter Fault Detection Method Based on Park Transformation and K-means Clustering Algorithm. In Proceedings of the CAA Symposium on Fault Detection, Supervision, and Safety for Technical Pro-cesses, Chengdu, China, 17–18 December 2021; pp. 1–6.
23. Lu, K.C.; Lin, F.J. Intelligent Power Control System of Three-Phase Grid-Connected PV System. Ph.D. Thesis, National Central University, Taiwan, 2015.

24. Sahoo, A.; Mahmud, K.; Ciobotaru, M.; Ravishankar, J. Adaptive Grid Synchronization Technique for Single-phase Inverters in AC Microgrid. In Proceedings of the IEEE Energy Conversion Congress and Exposition, Baltimore, MD, USA, 29 September–3 October 2019; pp. 4441–4446.
25. The Technical Highlights for Parallel Connection of Renewable Energy Power Generation System, Taiwan Power Company. Available online: https://www.taipower.com.tw/upload/228/2018120409203473289.pdf (accessed on 5 May 2022).